AIAA AVIATION Forum
5-9 June 2017, Denver, Colorado
47th AIAA Fluid Dynamics Conference

Effects of aspect ratio and angle of attack on tip vortex structures and aerodynamic performance for rotating flat plates

Chengyu Li[1], Haibo Dong[2]
Department of Mechanical and Aerospace Engineering
University of Virginia, Charlottesville, VA 22904

Bo Cheng[3]
Department of Mechanical and Nuclear Engineering
Pennsylvania State University, University Park, PA 16802

Numerical simulations are used to investigate the effects of aspect ratio and angle of attack on the vortex structure, circulation and aerodynamic performance of revolving wings at a low Reynolds number regime (200 ~ 1600). Rectangular wings with various aspect ratio (1 ~ 8) are considered and rotating from rest at angle of attack ranging from 15 to 90 degrees. Simulations are carried out using an in-house immersed-boundary-method-based direct numerical simulation (DNS) solver. A detailed analysis of the vortex formation shows that the general wake pattern near the wingtip shift from a single vortex loop to a pair of counter-rotating vortex loops. This tip vortex evolution was found related to the strength of LEV. In general, the stronger LEV will enhance the counter-pair trailing-edge vorticity. As the TEV increased, a secondary tip vortex will be formed at the bottom corner of wingtip and generate a pair of counter-rotating tip vortex loops. With the increment of the Reynolds number, these vortex loops will interact with each other and form hairpin-like vortical structures in the tail of the arc-shaped vortex loops. In addition to the vortex structures, the aerodynamic loading and power consumption were also examined. The findings from this work could be used to further understand the vortex dynamics of finite-aspect-ratio revolving wings at high angle of attack.

Nomenclature

AR	: Aspect ratio	Re	: Reynolds number
a	: Smoothing parameter	U_{tip}	: Wingtip velocity
b	: Span length	α	: Angle of attack
c	: Chord length	τ	: Non-dimensional time
R	: Radius from wingtip to rotational center	Ω_0^*	: Steady state angular velocity

I. Introduction

CONVENTIONAL fixed- and rotary-wing configurations adopt high aspect ratio wings to increase power economy, and operate the wings at low angle of attack to prevent flow separation and dynamic stall. Natural flyers, such as birds [1,2] and insects [3,4], equip low aspect ratio wings and flap their wings at high angle of attack without suffering any stalling. Instead, a stable attached leading-edge vortex (LEV) is generated when their wings translate in the stroke plane. Previous studies have demonstrated that some key aerodynamic features of flapping wings can be reproduced by revolving finite-aspect-ratio wings at

[1] Postdoctoral Researcher, li.7881@osu.edu, AIAA Member (current at The Ohio State University)
[2] Associate Professor, haibo.dong@virginia.edu, AIAA Associate Fellow (Corresponding Author)
[3] Assistant Professor, buc10@psu.edu, AIAA Member

high angle of attack [5-7]. For instance, Usherwood [8] experimentally studied a revolving dried pigeon wing and a flat card replica. The force measurements showed that revolving wings at higher geometric angle of attack ($43°$) can achieve much higher lift. The maximum lift coefficients of real and model wings can reach up to 1.64 and 1.44, respectively. In another study, the vortex structures of rotating flat-plates at various aspect-ratios (*AR*=2 and 4) have been investigated by Carr et al. [9] through stereoscopic digital particle image velocimetry (S-DPIV) techniques. It was found that, for *AR*=2, the aft-tilted LEV merged with the tip vortex (TV). For *AR*=4, the LEV and TV move past the trailing edge. Garmann and Visbal [10] numerically studied the vortex structures and aerodynamic loading of revolving wings. Their simulations illustrated that the pressure gradient force and the centrifugal force together were responsible for maintaining the attachment of LEV and avoiding the flow separation. Due to significant three-dimensional effects, the unsteady flow structure generated by low aspect ratio plates at low Reynolds number remains poorly understood.

The purpose of the present computational study aims to examine the vortex formation and aerodynamic performance of finite-aspect-ratio revolving wings in quiescent flow via a high-fidelity direct numerical simulation (DNS) in-house solver. The current study focuses on the effects of Reynolds number, wing aspect ratio and angle of attack on the tip vortex formation and aerodynamic performance of revolving wings. An outline of the chapter is given below. Section II gives a brief introduction to the numerical methodology and the simulation setup. Besides, the validity of the current solver is demonstrated by comparing with the experimental measurements. This is followed by a detailed discussion of the wake topology and aerodynamic performance in Section III. Finally, the conclusions are given in Section IV.

II. Methodology

A. Governing equation and numerical method

The numerical simulations are achieved by a second-order, Cartesian-grid-based immersed-boundary method. The detail of this solver has been described in Ref. [11], and only brief descriptions are provided here.

The non-dimensional equations governing the flow in the numerical solver are the time-dependent, viscous incompressible Navier-Stokes equations, written in indicial form as Eq. (1):

$$\frac{\partial u_i}{\partial x_i} = 0, \qquad \frac{\partial u_i}{\partial t} + \frac{\partial (u_i u_j)}{\partial x_j} = -\frac{\partial p}{\partial x_i} + \frac{1}{Re}\frac{\partial}{\partial x_j}\left(\frac{\partial u_i}{\partial x_j}\right) \tag{1}$$

where u_i ($i = 1,2,3$) are the velocity components in the x-, y- and z-directions, respectively; p is the pressure; and Re is the Reynolds number.

The above equations are discretized using a second-order central difference scheme on a non-uniform Cartesian mesh, where the velocity and pressure are collocated at the cell centers. The unsteady equations are solved using a fractional step method, which provides second-order accuracy in time. An Adams-Bashforth scheme and an implicit Crank-Nicolson scheme are employed for the discretization of the convective terms and diffusion terms, respectively. Boundary conditions on immersed bodies are imposed through a "ghost-cell" procedure. Flow simulations are conducted on stationary non-body-conformal Cartesian grids. This arrangement eliminates the need for the complicated re-meshing algorithms that are usually employed by conventional Lagrangian body-conformal methods. Additional flow validation for this code can be found in Ref. [12]. The current flow solver has also been used to simulate canonical flapping plates [13-17] and realistic insect wings [18-21].

B. Wing kinematics and simulation setup

The current study employs rectangular wing planform with aspect-ratio of *AR*=1, 2, 4 and 8, which is defined as $(\text{span})^2 / (\text{area})$, and the wing thickness is treated as 3% of the wing chord length. The wing surface is represented by a fine unstructured grid with triangular elements. The wing root is extended out a distance $0.5c$ away from the rotational axis at a range of angle attack (α) from 15 to 90 degrees. The revolving wing configuration is shown in Figure 1(a). The Reynolds number range selected in this paper is from 200 to 1600, which is defined as $Re = U_{tip}R/\nu$, based on the wingtip velocity and the rotational distance (*R*) between the wingtip and the rotational center. Table 1 provides a concise summary of all the parameters involved and their range.

The velocity profile used for the revolving wings consists of a piecewise linear function in three phases: an acceleration phase, a constant speed phase, and a deceleration phase. The acceleration and deceleration were chosen so that the speed increases linearly over 0.25c of travel at 75% of tip radius. The angular velocity profile is given by the following equation.

$$\Omega^*(\tau) = \begin{cases} \dfrac{\Omega_0^*}{2a(\tau_2 - \tau_1)} ln[\dfrac{cosh(a(\tau - \tau_1))}{cosh(a(\tau - \tau_2))}] + \dfrac{\Omega_0^*}{2}, & 0 \le \tau \le \dfrac{(\tau_2 + \tau_3)}{2} \\ \dfrac{\Omega_0^*}{2a(\tau_4 - \tau_3)} ln[\dfrac{cosh(a(\tau - \tau_3))}{cosh(a(\tau - \tau_4))}] + \dfrac{\Omega_0^*}{2}, & \tau \ge \dfrac{(\tau_2 + \tau_3)}{2} \end{cases} \quad (2)$$

where Ω_0^* is the steady state angular velocity; a is the smoothing parameter, τ_1 is the start time, τ_2 marks the end of the acceleration, τ_3 marks the beginning of the deceleration, and τ_4 marks the end of deceleration.

This expression is modified form of a function described by Eldredge et al. [22], which allows for a continuous motion that is sufficiently differentiable, thereby avoiding discontinuities in the angular acceleration. In current simulations, the value of smoothing parameter, a, is set to 30. Figure 1(b) shows the smoothed angular velocity profile. The dashed vertical line marks the acceleration duration ($\tau_2 - \tau_1$) and deceleration duration ($\tau_4 - \tau_3$).The wing is initially at rest in quiescent flow before accelerating to a constant rotational rate, and the total rotational angle is 8π (4 revolving cycles).

The computational domain size of the simulation is $30c \times 20c \times 30c$ in terms of wing chord length (c) to get domain independence results. To maintain consistent grid resolutions in both x- and z-directions, the nominal grid size employed in the current simulations range from $185 \times 129 \times 185$ for the smallest aspect ratio wing (*AR*=1) to $393 \times 137 \times 393$ for the largest aspect-ratio wing (*AR*=8). Figure 1(c) shows a typical grid used in the current study for *AR*=2. The domain mesh has two refined layers. As can be seen in this figure, very high resolution is provided in a cuboidal region around the plate in all three directions with the smallest resolution of $\Delta x = 0.03c$. Around this region, there is a secondary denser layer with $\Delta x = 0.05c$. Beyond the secondary denser layer, the grid is stretched rapidly. Boundary conditions along all sides of the computational boundary are setting as convective boundary condition. A homogeneous Neumann boundary condition is used for pressure at all these boundaries.

To quantify the aerodynamic performance, the force coefficients used in the current study are defined as $C_{L,D,\mathrm{N,T}} = (F_L, F_D, F_N, F_T)/0.5\rho U_{tip}^2 S$, in which F_L, F_D, F_N, and F_T are lift, drag, normal, and tangential force, respectively, ρ is the density of the fluid, and S is the area of the wing. The aerodynamic power is defined as $C_{PW} = P/0.5\rho U_{tip}^3 S$, where P is the aerodynamic power consumption. The instantaneous

aerodynamic power (P) is defined as the surface integration of the inner product between the pressure and the velocity in each discretized element.

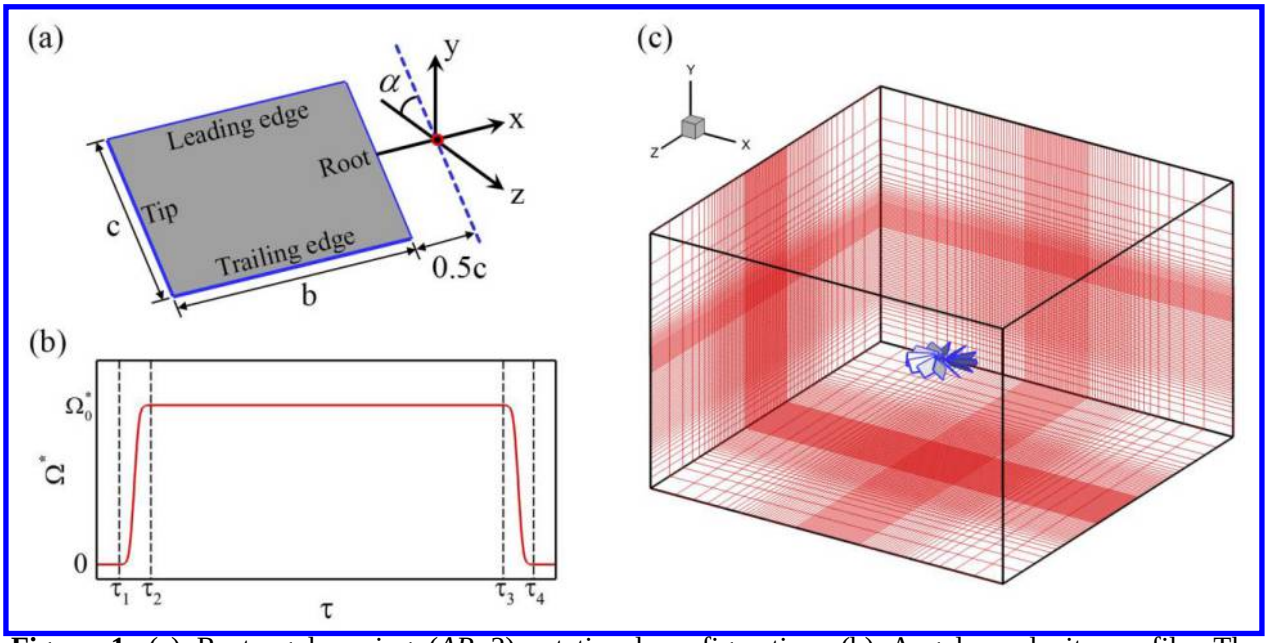

Figure 1. (a) Rectangular wing (*AR*=2) rotational configuration. (b) Angular velocity profile. The duration between dashed lines indicate the acceleration/deceleration phases. (c) Computational domain and mesh employed in the simulation of *AR*=2 rectangular wing.

Table 1. Parameters involved in the current study and their ranges.

AR	Re_{tip}	α
1, 2, 4, 8	200, 400, 800, 1600	15°, 30°, 45°, 60°, 75°, 90°

C. Solver validation

Revolving wing experiments [23] were performed in a $18\text{in}\times 18\text{in}\times 18\text{in}$ glass tank filled with mixing water/glycerin. The geometry considered in this study is an aspect-ratio-two rectangular wing. The root of the wing is extended out a distance of $0.5c$ from the rotation axis at a fixed angle of attack $45°$. The wing kinematics profile is similar as the one used in the current study, and the total rotational angle is $720°$. The Reynolds number for this case equals to 500.

As shown in Figure 2, the force coefficients experienced a sharp peak associated with the inertial forces, followed shortly by a second peak. In general, our simulation results have a good agreement with the experimental measurements.

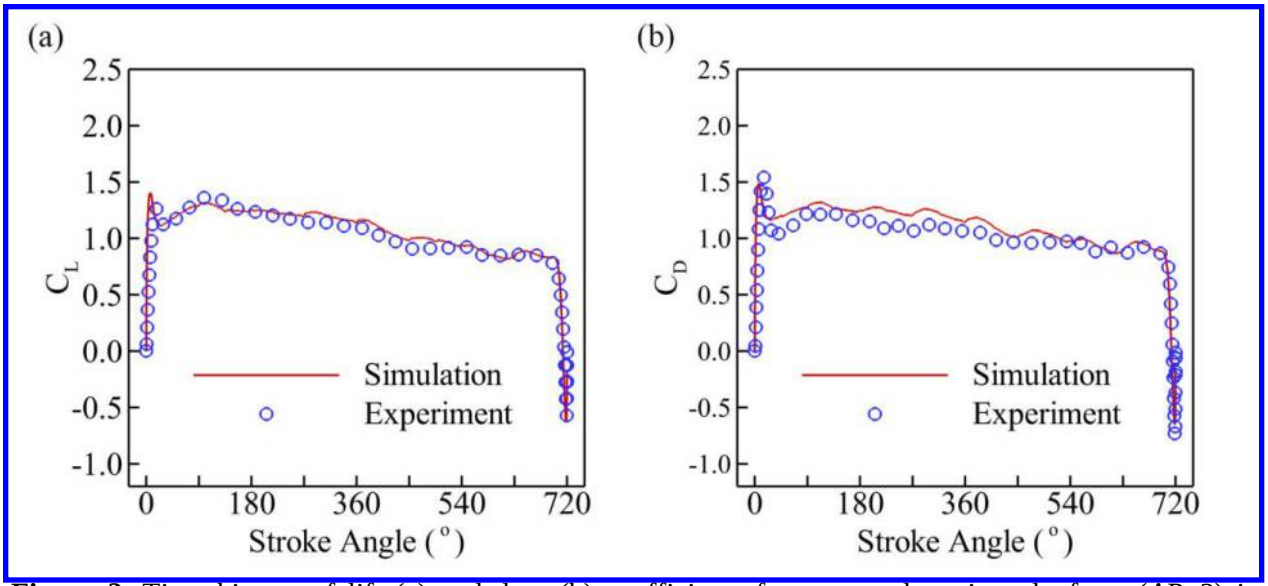

Figure 2. Time history of lift (a) and drag (b) coefficients for rectangular wing planform (*AR*=2) in rotational motion at *Re*=500. The experimental data are reproduced from Ref. [23].

III. Results and Discussion

In this section, we first present the tip vortex formation of a rectangular flap wing with *AR*=2 and α=45° undergoing a rotational motion at the wingtip Reynolds number ranging from 200 to 1600. Following this discussion, the effect of the aspect ratio and angle of attack on the vortex structure and associated aerodynamic performance are discussed for the range of parameters listed in Table 1.

A. Wingtip vortex formation of the baseline case at various Reynolds number

To paint a clear picture of the three-dimensional flow structure around wingtip, the revolving wing has been simulated for a range of Reynolds number, $200 \le Re \le 1600$. Figure 1 (a-b) illustrates the effect of the Reynolds number on the lift and drag coefficients of the wing (*AR*=2) at a fixed angle of attack $45°$. The grey shaded area indicates the period of the acceleration phase. It can be seen that all of the curves are characterized by an initial steep increase in the force coefficients, leading to a peak followed by a sharp drop and subsequent recovery to an intermediate level. The magnitudes of initial force peaks are identical for all the curves, but the force magnitude after recovery are different. It appears that the higher Reynolds number leads to a higher force magnitude after recovery, but has no significant effect during the acceleration phase when inertial force plays a dominant role. Once the wing rotates approximate 90 degrees, the force coefficients reach a steady-state value.

The vortex structures at various Reynolds number are shown in Figure 1 (c), when the force coefficients reach a steady-state value. The stroke angle of the wing is indicated by the black dashed line in Figure 1 (a-b). Two iso-surfaces are shown to highlight the inner core (red) and outer shell (grey) of the vortex structure. At *Re*=200, the primary vortex structures, such as leading-edge vortex (LEV), root vortex (RV), tip vortex (TV), can be identified easily. In addition to the TV located at the top corner of the tip, there is also a secondary tip vortex (STV) generated from the bottom corner of the tip. Due to the viscous dissipation effect, these vortex structures are simple and neat. As the Reynolds number increased to 400, all the vortex structures observed in *Re*=200 case are preserved and strengthen as indicated by the thicker red core iso-surface. When both TV and STV become stronger, the tail of these vortex loops start

to interact with each other and form a hairpin-like vortex in the far wake. This interaction become much stronger as the *Re* further increased to 800. The LEV also starts to left up from the wing surface and burst when it closes to the wingtip. At *Re*=1600, the instability of the vortex around the wingtip is further amplified. Most of the vortex structures become chaotic and only leave the LEV can be identified.

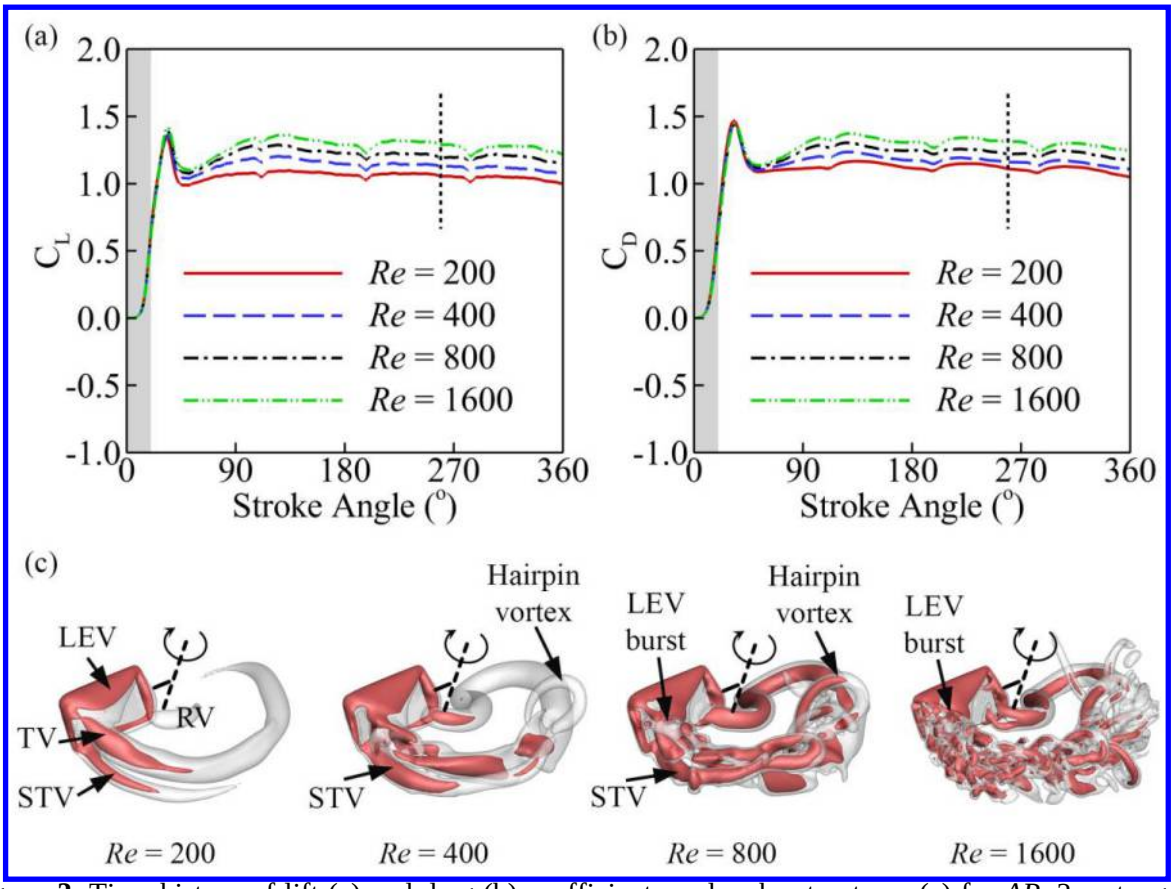

Figure 3. Time history of lift (a) and drag (b) coefficients and wake structures (c) for *AR*=2 rectangular wings at various Reynolds number (*Re*) with a fixed angle of attack of $45°$. The shaded region indicates the acceleration phases. The black dashed line in plots (a-b) denotes the stroke angle of the wake structures shown in plot (c).

B. Effects of *AR* at constant Reynolds number

In this section, we examined the effect of wing aspect ratio on the wake topology and aerodynamic performance of the rectangular flat wing at *Re*=200 with a fixed angle of attack $45°$. The simulations were running for 4 revolving cycles to ensure that the flow reaches a periodical stage. Figure 4 shows the vortex structures of different aspect-ratio wings at $\tau = 3.5$. The vortex structures are visualized by the Q-criterion with the iso-surface value Q=8 (in grey) for indicating the shell of the vortex structures. As shown in Figure 4, LEV and TV develop and connect smoothly along the wing span direction. The size of the vortex loop increases with aspect ratio since the travel distance at the wingtip also scales with span, but the overall development of the vortex system is similar for each aspect ratio. A detailed analysis of the vortex formation shows that the general wake pattern near the wingtip shift from a single vortex loop for lower aspect-ratio cases (*AR*=1) to a pair of counter-rotating vortex loops for higher aspect-ratio cases (*AR*=2, 4 and 8).

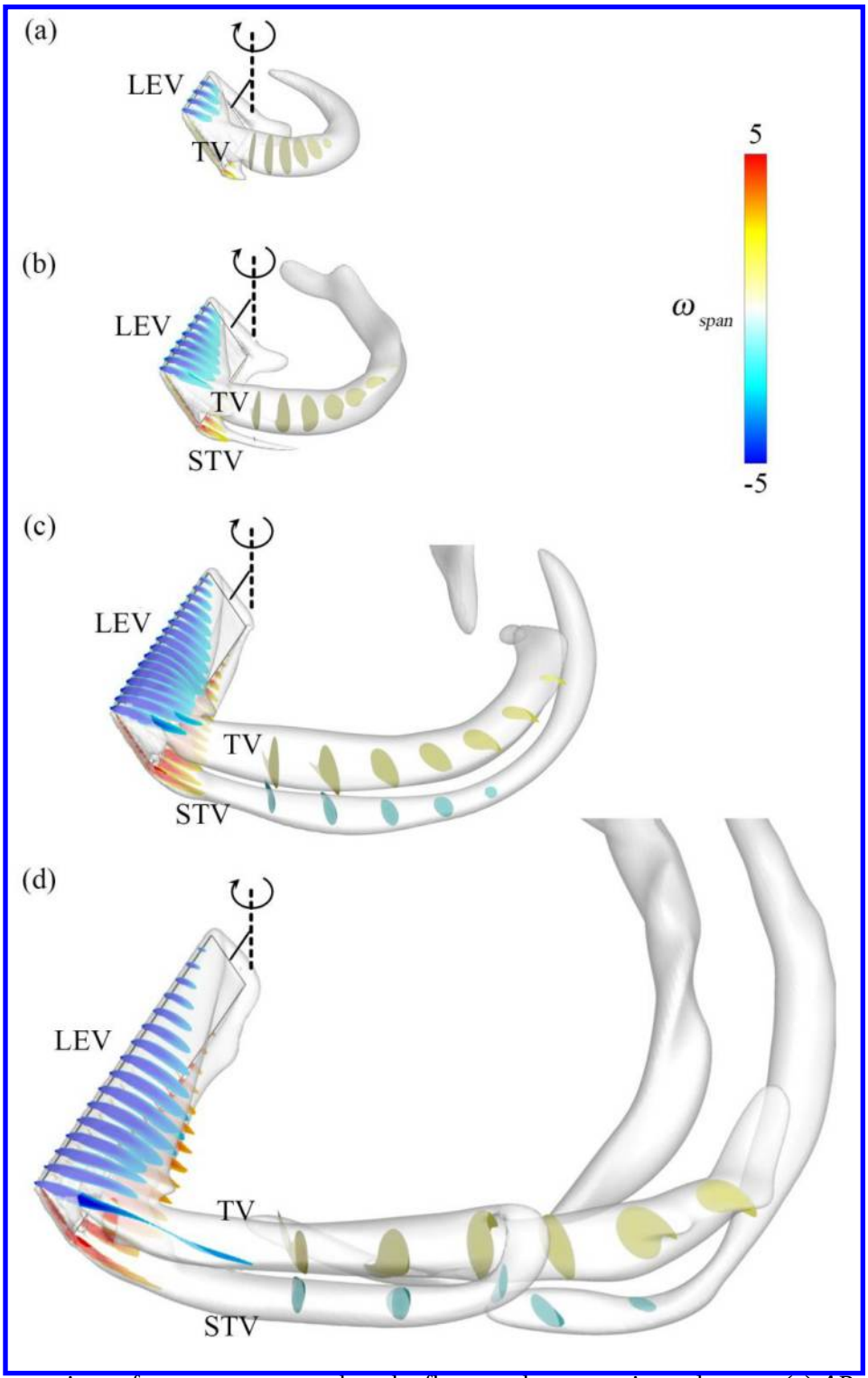

Figure 4. Comparison of vortex structure when the flow reaches a quasi-steady state. (a) *AR*=1. (b) *AR*=2. (c) *AR*=4. (d) *AR*=8. The vortex structures are visualized using Q-criterion. The leading-edge vortex (LEV), trailing-edge vortex (TEV), tip vortex (TV), and secondary tip vortex (STV) are colored by spanwise vorticity.

To quantify the strength of the LEV, we further visualize the vorticity field using contour lines. After each vortex is manually identified, a closed contour line is generated around this vortex with a specified level, and the circulation (Γ) is then calculated by integrating along this line. Although the magnitude of the circulation depends on the chosen contour level, the characteristic behavior of the vortex is not affected by this choice.

Figure 5 shows a comparison of LEV circulation along wing span for various aspect-ratio wings. The vortex circulation is normalized by $U_{tip}c$. In general, the circulation of LEV increases approximately linearly up to70% wing span and then starts to decrease due to the split of LEV near the wingtip. For high aspect-ratio wings, however, the LEV circulation raise again at about 85% spanwise locations. In addition, the LEV of low aspect-ratio wings has relative higher strength near the wing root.

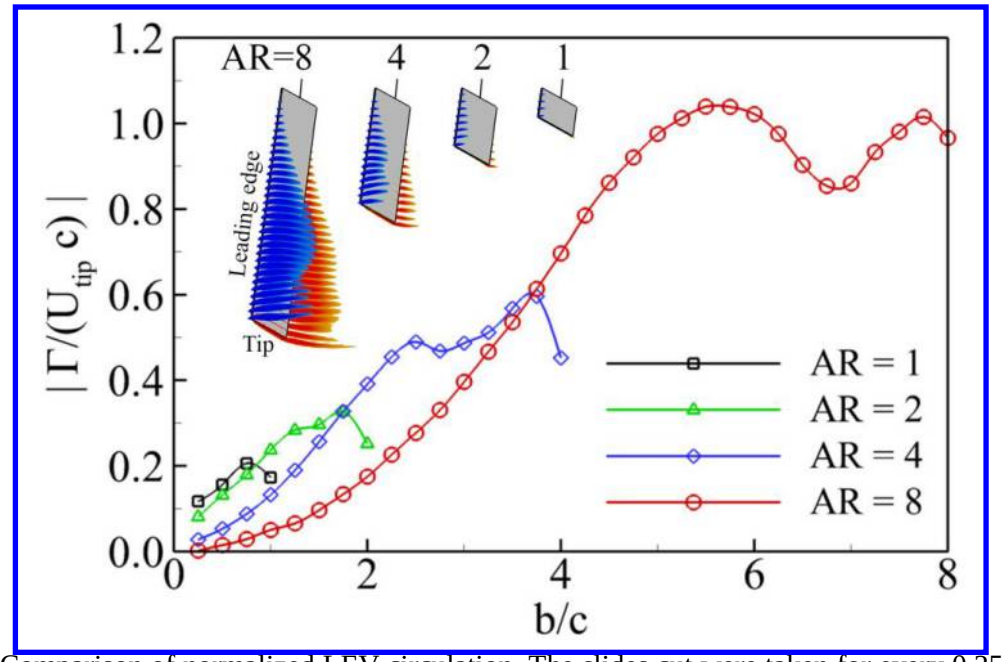

Figure 5. Comparison of normalized LEV circulation. The slides cut were taken for every 0.25*c* from the wing root to wingtip for all revolving wings.

Figure 6 shows the time course comparison of forces and aerodynamic power coefficients of wings with AR=1, 2, 4 and 8 in a complete four rotational cycles. During the rotational motion, the instantaneous aerodynamic performance of each aspect ratio case shares the similar decreasing and increasing tendency and gradually reach to a constant value once the flow reaches a nearly stationary state. At the first rotational cycle, both aerodynamic force and power coefficients are shown a larger value due to the impulsive start. The similar observation also presented in Ref. [24] by comparing the revolving motion and flapping motion for a pair of hawkmoth wing model. In current study, the mean value of forces and power coefficients, lift-to-drag ratio, lift-to-power-ratio, and normal force-to-power-ratio are shown in Figure 7. Although the *AR*=1 case owns a relative higher lift coefficient, the increment of aspect-ratios can improve the aerodynamic efficiency in terms of lift-to-drag ratio, lift-to-power ratio, and normal force-to-power-ratio. The optimal case is the wing with *AR*=2.

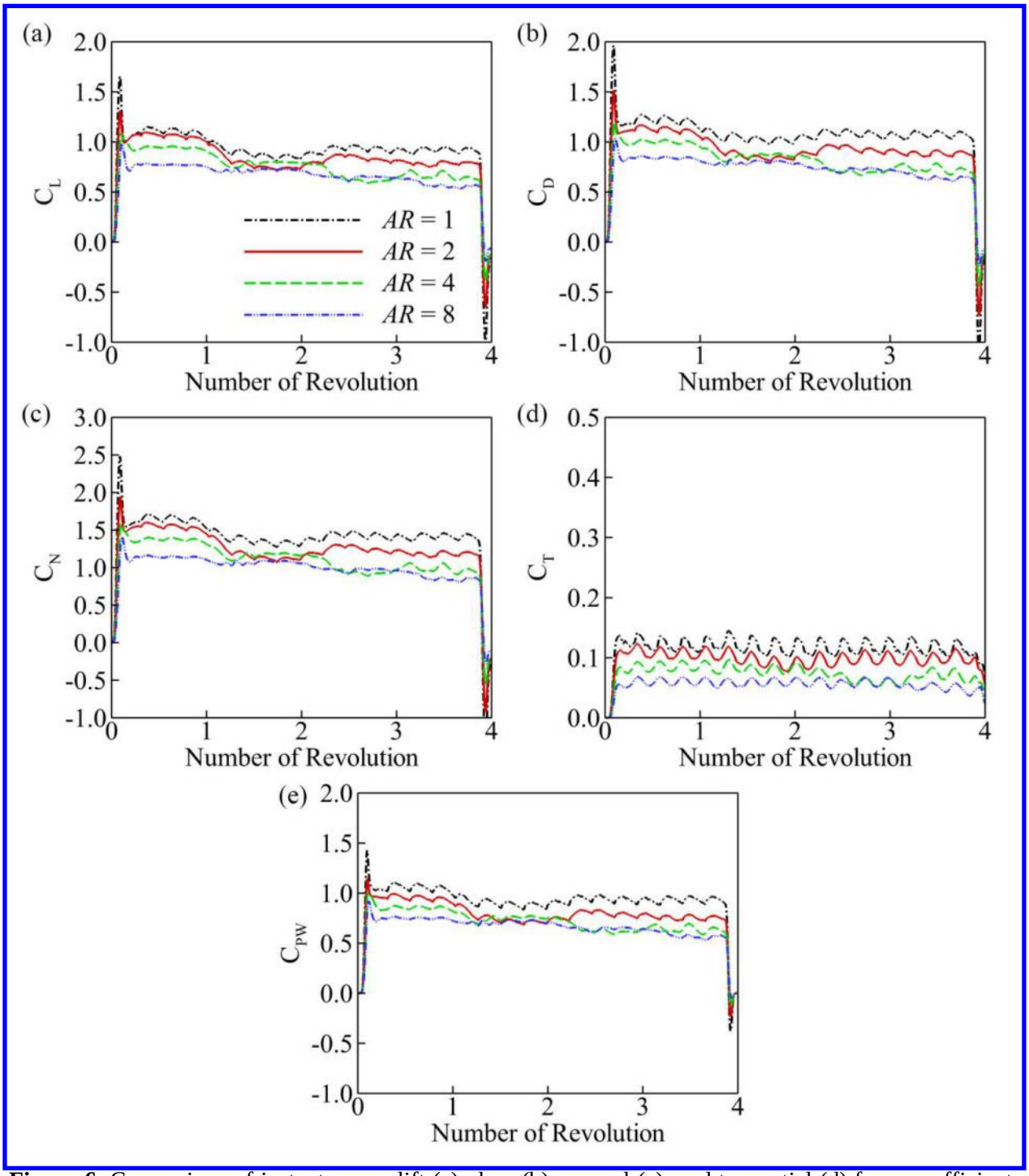

Figure 6. Comparison of instantaneous lift (a), drag (b), normal (c), and tangential (d) force coefficients and aerodynamic power coefficient (e) for wings with different aspect-ratio at $\alpha = 45°$ and *Re* = 200, during four revolving cycles.

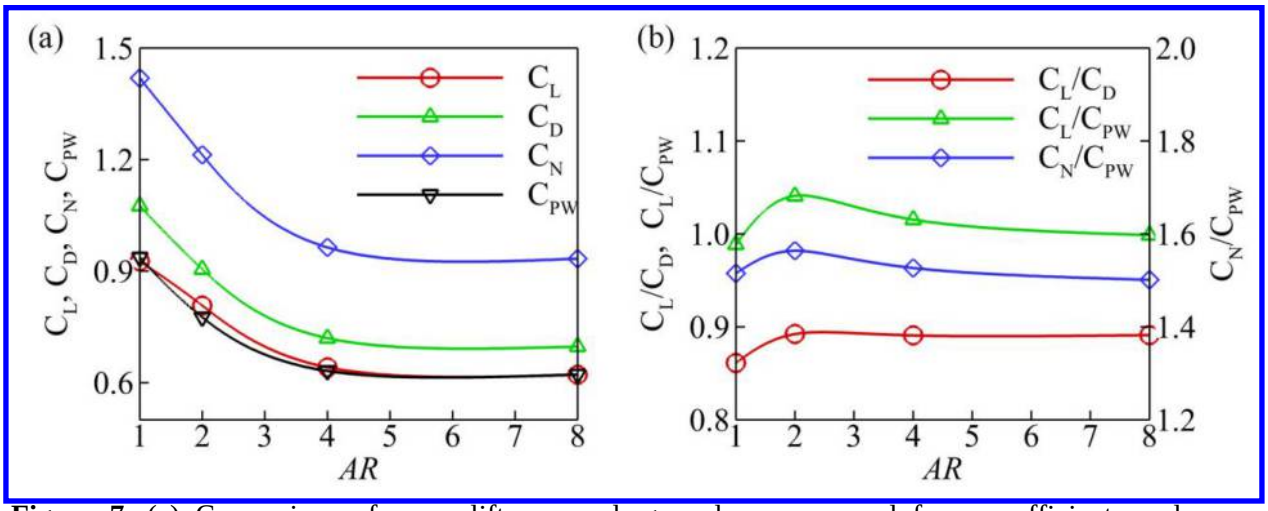

Figure 7. (a) Comparison of mean lift, mean drag, and mean normal force coefficients and mean aerodynamic power coefficient for wings at different aspect-ratios. (b) Comparison of lift-to-drag ratio, lift-to-power ratio, and normal force-to-power ratio for wings at different aspect-ratios. The angle of attack and tip Reynolds numbers for all the cases are fixed at $45°$ and 200, respectively. The forces and power coefficients were averaged over the last two revolving cycles.

C. Effects of angle of attack at constant Reynolds number

In this section, we examined the effect of the angle of attack on the wingtip vortex structure and aerodynamic performance for an *AR*=2 wing at *Re*=200. Figure 8 shows the evolution of the wingtip vortex with the changing of the angle of attack and its associated surface pressure distribution on the suction side of the wing. It can be seen that there is only one vortex loop formed around the wingtip at lower angle of attack ($\alpha = 15°$ and $30°$). As the α increased to $45°$, a tiny STV starts to develop from the bottom corner of the wingtip. This might be due to the enhancement of the trailing-edge vortex (TEV) at higher angle of attack. As the continuous increasing of α, ranging from $45°$ to $75°$, the STV becomes stronger and has the same magnitude with TV when the α reach $90°$. The proximity of the vortex to the surface of the wing promotes a strong region of suction along the leading-edge (dark blue region on the surface contour). For the lower α cases ($15°$ and $30°$), the suction region expand along the leading-edge direction and covers the wingtip region. As the α increasing, the vortex lifts off the surface into an arch-type structure as it reorients itself along the tip, which reduces the suction near the tip, as shown for $\alpha = 45°$ and $60°$. Once the α continuously increased, the LEV begins to entrain reversed-signed vorticity from the trailing-edge, which promotes outboard separation and lead to a further loss of suction near the tip, such as $\alpha = 75°$ and $90°$ cases.

In conjunction with the last section (Sec. III B), it appeases that the STV has a strong correlation with the strength of the TEV. Similar to the LEV, TEV also has its own vorticity, and its strength will be amplified with the increment of *AR* and/or α. Once the strength of TEV is enhanced, it will form its own trail of the vortex loop around the wingtip.

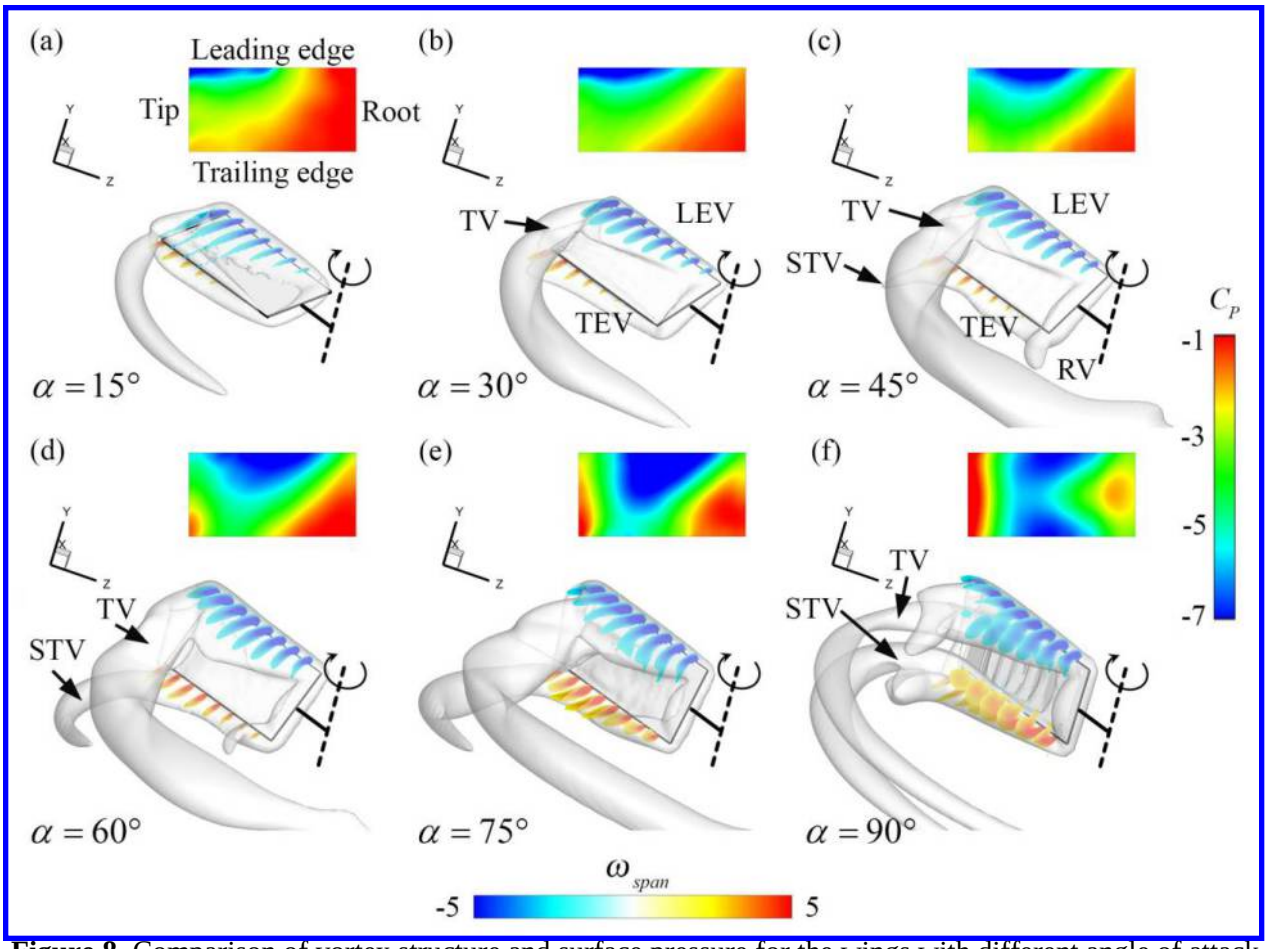

Figure 8. Comparison of vortex structure and surface pressure for the wings with different angle of attack when the flow field reached a quasi-steady state. (a) α = 15°. (b) α = 30°. (c) α = 45°. (d) α = 60°. (e) α = 75°. (f) α = 90°. The vortex structures are visualized using Q-criterion. The leading-edge vortexes (LEV), trailing-edge vortexes (TEV) are colored by spanwise vorticity. The normalized pressure was defined as $C_P = 2(p - p_\infty)/(\rho U_{tip}^2)$.

To illustrate the effect of angle of attack on the LEV, Figure 9 shows the LEV circulation along wing span as the vortex formation reach a steady state. Before each LEV circulation curve reaches its own maximum value, the slope of each curve gradually increasing with the angle of attack. In addition, the peak value that can be reached for different cases is similar (the normalized circulation ~ 0.3). Once the strength of LEV reaches this peak, its strength will decay along the spanwise direction. The only exception is the case with $\alpha = 15°$, which has a much less peak value and without showing any decreasing trend on the LEV circulation along the spanwise direction.

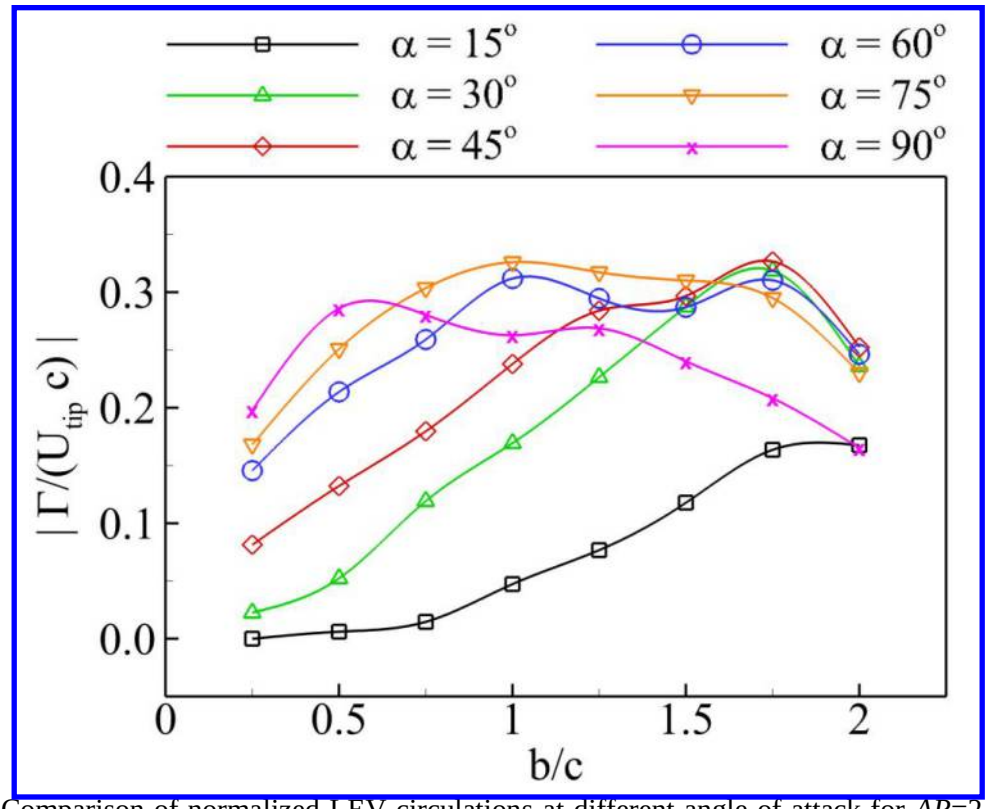

Figure 9. Comparison of normalized LEV circulations at different angle of attack for *AR*=2 rectangular wings. The slides cut were taken for every 0.25*c* from the wing root to wingtip.

Figure 10 shows the temporal variation in the forces and power coefficients over the entire four revolving cycles. The lift coefficient increases before the angle of attack reach to $45°$, and then decreases as the angle of attack continuously increasing. The other force coefficients, such as drag, normal, and tangential forces, present a linear trend of increment as the angle of attack. The variation in the mean force and power coefficients and aerodynamic efficient ratio are shown in Figure 11. It can be observed from this figure that the drag and normal forces and power coefficients monotonically increases with the angle of attack. The maximum value of the lift is reached at α between $30°$ and $45°$. Furthermore, the $\alpha = 30°$ case has the best overall aerodynamic efficiency for the cases simulated in the current section.

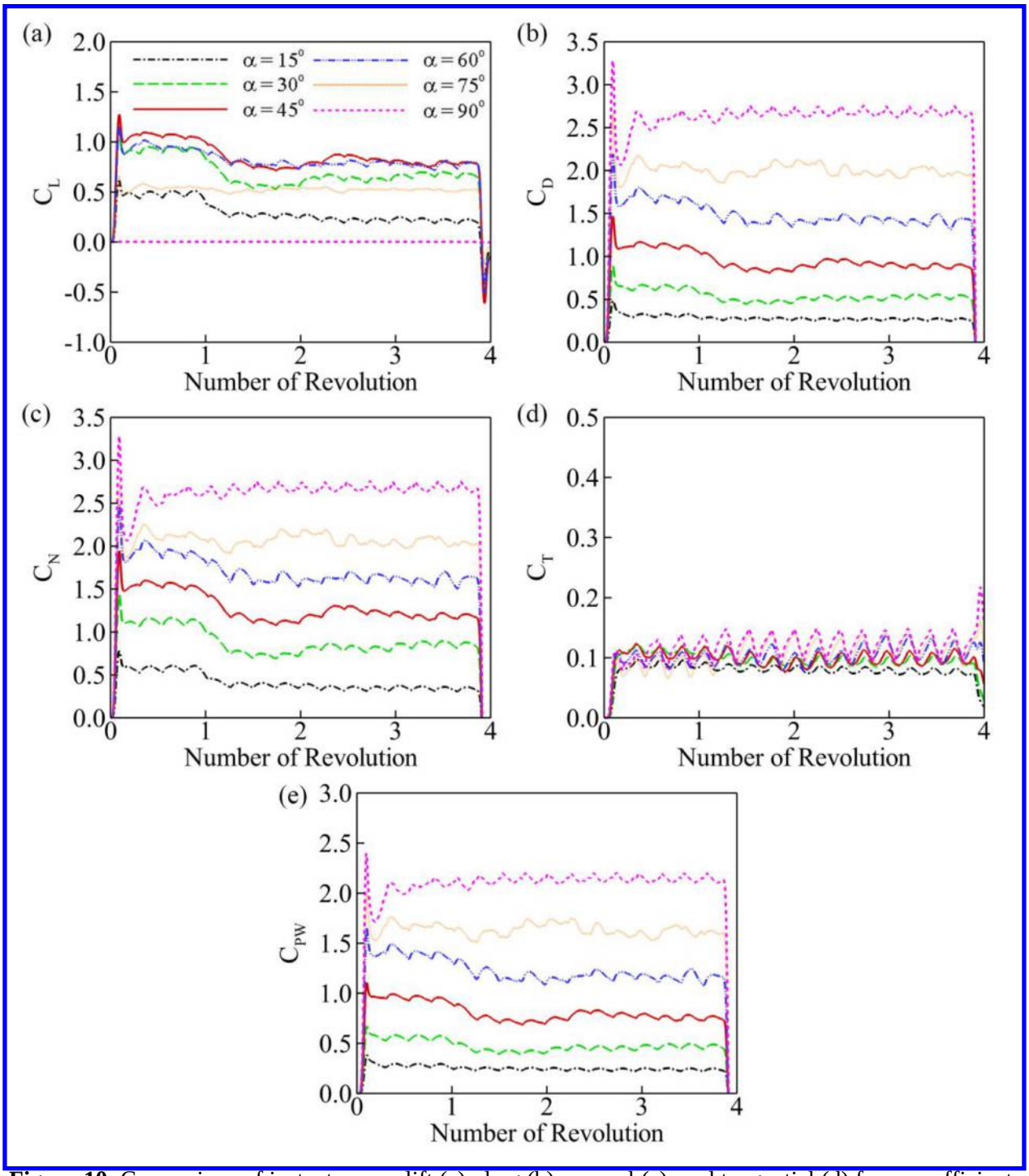

Figure 10. Comparison of instantaneous lift (a), drag (b), normal (c), and tangential (d) force coefficients and aerodynamic power coefficient (e) for wings at different angle of attack with *AR* = 2 and *Re* = 200, during four revolving cycles.

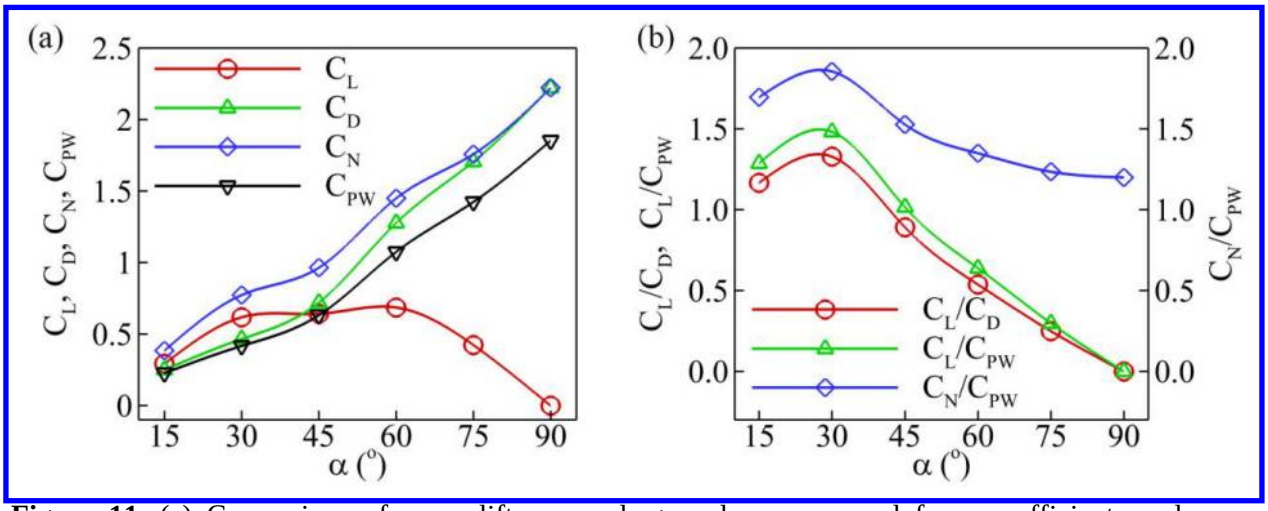

Figure 11. (a) Comparison of mean lift, mean drag, and mean normal force coefficients and mean aerodynamic power coefficient for wings at different angle of attack. (b) Comparison of lift-to-drag ratio, lift-to-power ratio, and normal force-to-power ratio for wings at different angle of attack. The wing aspect-ratio and tip Reynolds numbers for all the cases are fixed at 2 and 200, respectively. The forces and power coefficients were averaged over the last two revolving cycles.

IV. Conclusion

High-fidelity numerical simulations have been conducted to examine the vortex structure and aerodynamic loading on revolving wings over a range of Reynolds number, aspect ratios, and angle of attack. The simulations have shown that for the cases with lower strength of the LEV and TEV, there was only a single TV loop near the top corner of the wingtip. With the increment of the LEV strength either due to higher aspect ratios ($AR > 1$) or higher angle of attacks ($\alpha > 30°$), a STV would be formed near the bottom corner of the wingtip. The formation of this STV was likely due to the enhancement of the TEV. The TV and STV together form a pair of counter-rotating vortex loops around the wingtip, which could interact with each other and form a hairpin-like vortex structure once the Reynolds number increased above 200.

The instantaneous forces and aerodynamic power coefficients were also evaluated. An initial peak was observed for all simulations right after the acceleration phase due to the impulsive start. Following this initial peak, the forces and power coefficients experience a sharp drop and recover to an intermediate value for the remainder of the first evolution. After the wing enters the second revolution, both forces and power coefficients drop and level out to a lower value comparing with the first revolving cycle. The mean forces and power coefficients showed that the maximum lift and efficiency can be reach for the wing with AR=2 with angle of attack around 30~45 degrees at Re=200.

Acknowledgments

This research is supported by NSF grant CBET-1313217, AFOSR grant FA9550-12-1-0071 and ONR MURI grant N00014-14-1-0533.

References

[1] Cheng B, Tobalske B W, Powers D R, Hedrick T L, Wang Y, Wethington S M, Chiu G T-C and Deng X 2016 Flight mechanics and control of escape manoeuvres in hummingbirds II. Aerodynamic force production, flight control and performance limitations *J. Exp. Biol.* jeb. 137570.

[2] Cheng B, Tobalske B W, Powers D R, Hedrick T L, Wethington S M, Chiu G T and Deng X 2016 Flight mechanics and control of escape manoeuvres in hummingbirds I. Flight kinematics *J. Exp. Biol.* jeb. 137539.

[3] Li C and Dong H 2017 Wing kinematics measurement and aerodynamics of a dragonfly in turning flight *Bioinspir. Biomim.* **12** 026001.

[4] Koehler C, Wischgoll T, Dong H and Gaston Z 2011 Vortex Visualization in Ultra Low Reynolds Number Insect Flight *IEEE Trans. Vis. Comput. Graphics* **17** 2071-2079.

[5] Usherwood J R and Ellington C P 2002 The aerodynamics of revolving wings - I. Model hawkmoth wings *J. Exp. Biol.* **205** 1547-1564.

[6] Jones A R and Babinsky H 2010 Unsteady Lift Generation on Rotating Wings at Low Reynolds Numbers *J. Aircr.* **47** 1013-1021.

[7] Li C and Dong H 2014 Wake Structure and Aerodynamic Performance of Low Aspect-Ratio Revolving Plates at Low Reynolds number *AIAA Paper 2014-1453*.

[8] Usherwood J R 2009 The aerodynamic forces and pressure distribution of a revolving pigeon wing *Experiments in fluids* **46** 991-1003.

[9] Carr Z R, DeVoria A C and Ringuette M J 2015 Aspect-ratio effects on rotating wings: circulation and forces *J. Fluid Mech.* **767** 497-525.

[10] Garmann D and Visbal M 2014 Dynamics of revolving wings for various aspect ratios *J. Fluid Mech.* **748** 932-956.

[11] Mittal R, Dong H, Bozkurttas M, Najjar F M, Vargas A and von Loebbecke A 2008 A versatile sharp interface immersed boundary method for incompressible flows with complex boundaries *J. Comput. Phys.* **227** 4825-4852.

[12] Li C, Dong H and Liu G 2015 Effects of a dynamic trailing-edge flap on the aerodynamic performance and flow structures in hovering flight *J. Fluids Struct.* **58** 49-65.

[13] Li C and Dong H 2016 Three-dimensional wake topology and propulsive performance of low-aspect-ratio pitching-rolling plates *Phys. Fluids* **28** 071901.

[14] Xu M, Wei M, Li C and Dong H 2015 Adjoint-based optimization of flapping plates hinged with a trailing-edge flap *Theor. Appl. Mech. Lett.* **5** 1-4.

[15] Wan H, Dong H, Li C and Liang Z 2012 Vortex Formation and Aerodynamic Force of Low Aspect-Ratio Plate in Translation and Rotation *AIAA Paper 2012-3278*.

[16] Li C, Dong H and Ren Y 2014 A Numerical Study of Flapping Plates Hinged with a Trailing-Edge Flap *AIAA Paper 2014-2049*.

[17] Li C and Dong H 2016 Quantification and Analysis of Propulsive Wake Topologies in Finite Aspect-Ratio Pitching-Rolling Plates *AIAA Paper* 2016-4339.

[18] Wan H, Dong H and Gai K 2015 Computational investigation of cicada aerodynamics in forward flight *J. R. Soc. Interface* **12** 20141116.

[19] Liu G, Dong H and Li C 2016 Vortex dynamics and new lift enhancement mechanism of wing-body interation in insect forward flight *Journal of Fluid Mechanics* **795** 634-651.

[20] Li C, Wang J and Dong H 2017 Proper Orthogonal Decomposition Analysis of Flapping Hovering Wings *AIAA Ppaer 2017-0327*.

[21] Li C, Dong H and Liang Z 2016 Proper Orthogonal Decomposition Analysis of 3-D Wake Structures in a Pitching-Rolling Plate *AIAA Paper 2016-2071*.
[22] J. Eldredge C W, and M. Ol 2009 A computational study of a canonical pitch-up, pitch-down, wing maneuver *AIAA Paper 2009-3687*.
[23] Manar F a J, Anya R., The Eect of Tip Clearance on Low Reynolds Number Rotating Wings, AIAA Aerospace Sciences Meeting, National Harbor, Maryland, January, 2014.
[24] Zheng L, Hedrick T and Mittal R 2013 A comparative study of the hovering efficiency of flapping and revolving wings *Bioinspir. Biomim.* **8**.